Supplementary Information

Tuning Electrochemical Water Oxidation towards Ozone Evolution by Heterojunction Anode Architectures

Seok Kim [a], Seokhyun Choung [b], Woonghee Lee [a], Sungho Bae [a], Jeong Woo Han*[b], Kangwoo Cho*[a,c]

[a] Division of Environmental Science and Engineering, Pohang University of Science and Technology (POSTECH), Pohang 37673, Republic of Korea.

[b] Department of Chemical Engineering, Pohang University Science and Technology (POSTECH), Pohang 37673, Republic of Korea

[c] Institute for Convergence Research and Education in Advanced Technology, Yonsei University International Campus, Incheon 21983, Republic of Korea

*Co-corresponding author (J. W. Han);
Tel.: +82542792338; Fax: +82542795528; E-mail address: jwhan@postech.ac.kr

*Corresponding author (K. Cho);
Tel.: +82542792289; Fax: +82542798299; E-mail address: kwcho1982@postech.re.kr

Table of contents
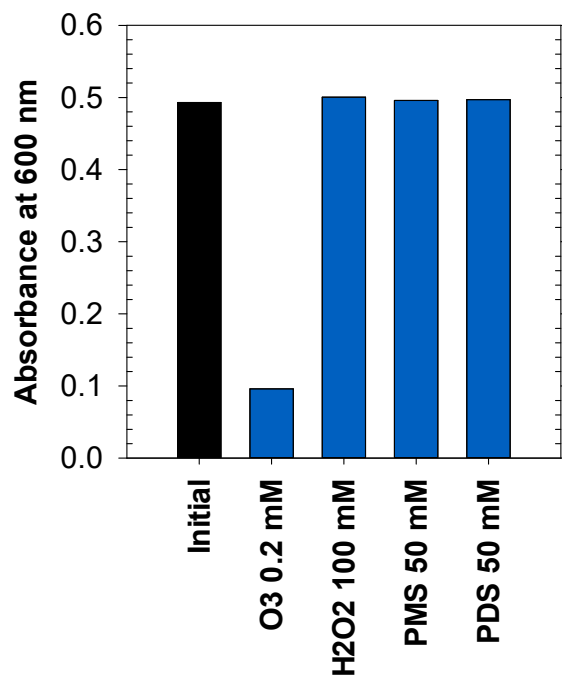
1. Galvanostatic ozone evolution

Fig. S1. Effects of oxidants that can be generated during the OZER, *i.e.* O$_3$, H$_2$O$_2$, peroxymonosulfate (PMS), and peroxydisulfate (PDS) on the absorbance in the indigo method. The indigo dye was selectively decolorized only by ozone.
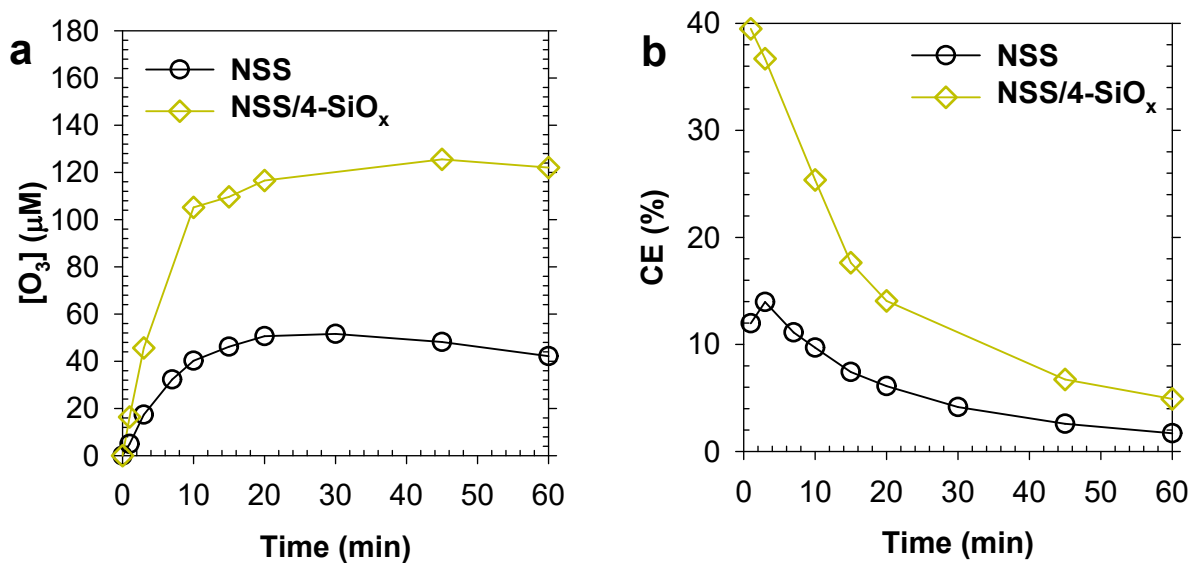
Fig. S2. Ozone concentration and OZER current efficiency under galvanostatic electrolysis over 1 h for NSS and NSS/4-MO$_x$ anodes; electrolyte = 0.5 M H$_2$SO$_4$, counter electrode = Pt, reference electrode = Ag/AgCl (3 M NaCl), j = 10 mA cm$^{-2}_{geo}$ (geometric area of anode = 2×2 cm^2).

The current efficiency (CE) of ozone evolution reaction (OZER) monotonically decreased (Fig. S2b) in a single-compartment cell under room temperature, engendered by the inevitable losses of dissolved ozone by self-decay (half-life ~ 15 min at pH 7 and 25 °C), volatilization, and reduction on cathodes. In this study, we focused on the initial CE values evaluated at 3 min, since the above interferences should be averted in the presence of aqueous pollutants, upon application in water treatment processes with *in-situ* OZER; *i.e.*, the generated O$_3$ would be immediately consumed by electron-donating pollutants. Nevertheless, a more precise estimation on CE would require divided cell experiments with flow electrolyte and/or measurements of gaseous O$_3$ in head-space, which necessitate further study.
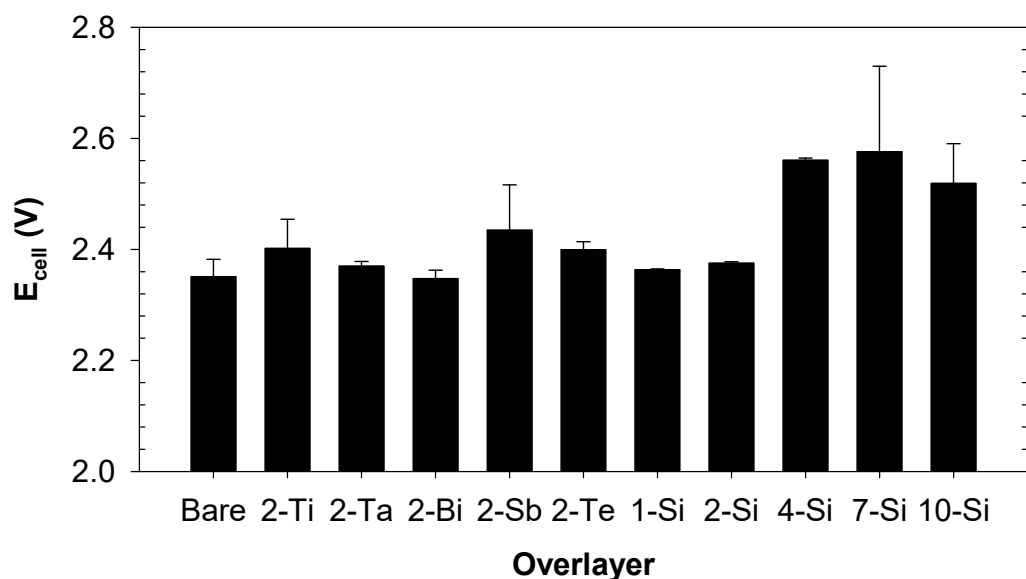
Fig. S3. Cell voltage (E_{cell}) of NSS/n-MO$_x$ anodes (n: number of coating cycle) under galvanostatic electrolysis presented in Fig. 1; electrolyte = 0.5 M H_2SO_4, counter electrode = Pt, reference electrode = Ag/AgCl (3 M NaCl), j = 10 mA cm$^{-2}_{geo}$ (geometric area of anode = 2×2 cm^2).

2. Stability test

SEM and XPS analyses on post-OZER samples were conducted to evaluate electrochemical stability after the SiO$_x$ overcoating. The SEM image of the NSS sample (Fig. S4a) shows that the surface was subject to spalling as the fractures were expanded after the OZER, in comparison with that of the pristine one (Fig. S13). In contrast, the surface of NSS/SiO$_x$ was relatively well preserved after the OZER. The XPS spectra in Fig. S4b also exhibit that the SiO$_x$ overlayer reduced the amount of alternation in the binding energy of the Sn cation, a main active site, indicating the SiO$_x$ overlayer enhanced electronic-structural stability of catalysts.[1] In addition, the dissolution of metal ions from catalyst after the OZER was quantified by inductively coupled plasma-optical

emission spectrometry (ICP-OES) in Table S1. The dissolution of metal ions was also significantly diminished on NSS/SiO$_x$ than bare NSS.

For accelerated life tests, constant j of 100 mA cm$^{-2}_{geo}$ was applied to comparatively evaluate the durability in terms of the electrolysis duration until the anodic potential reached 10 V$_{RHE}$ (Fig. S5). The anodic potential of NSS reached 10 V$_{RHE}$ within 0.5 h, whereas the NSS/SiO$_x$ lasted up to 2.5 h. The service life under the typical operating condition (j = 10 mA cm^{-2}) can be estimated to 25 h and 125 h for NSS and NSS/SiO$_x$, respectively, according to the empirical proportionality to $j^{1/m}$ (m ranges from 1.4 to 2.0, herein the averaged value of 1.7 was used).[2] The anode deactivation pathways could include physical loss (detachment[3, 4] and/or dissolution[5, 6]) of catalysts and passivation layer formation at interfaces of substrate/catalyst[7, 8] or catalyst/electrolyte.[9-11] The deterioration of NSS anode stability has mostly been ascribed to insulating TiO$_2$ formations on Ti substrates because the electrolyte could penetrate through surface cracks and pinholes of the NSS layer to oxidize the substrate.[9-11] The as-prepared NSS layer indeed carried loads of surface cracks, which were notably reduced by the SiO$_x$ overcoating (Fig. S13). A diminished exposure of Ti substrate was also confirmed by XPS as shown in Fig. 4a. The increased longevity, therefore, would be ascribed to a shielding effect of the SiO$_x$ overlayer, which is robust under an acidic environment as envisaged by the Pourbaix diagram.[12] Consequently, the NSS/SiO$_x$ anodes were corroborated to enhance anodic stability 4.7-fold than bare NSS. Note that the lifetime should be by far extended in realistic water treatment conditions under circum-neutral pH.
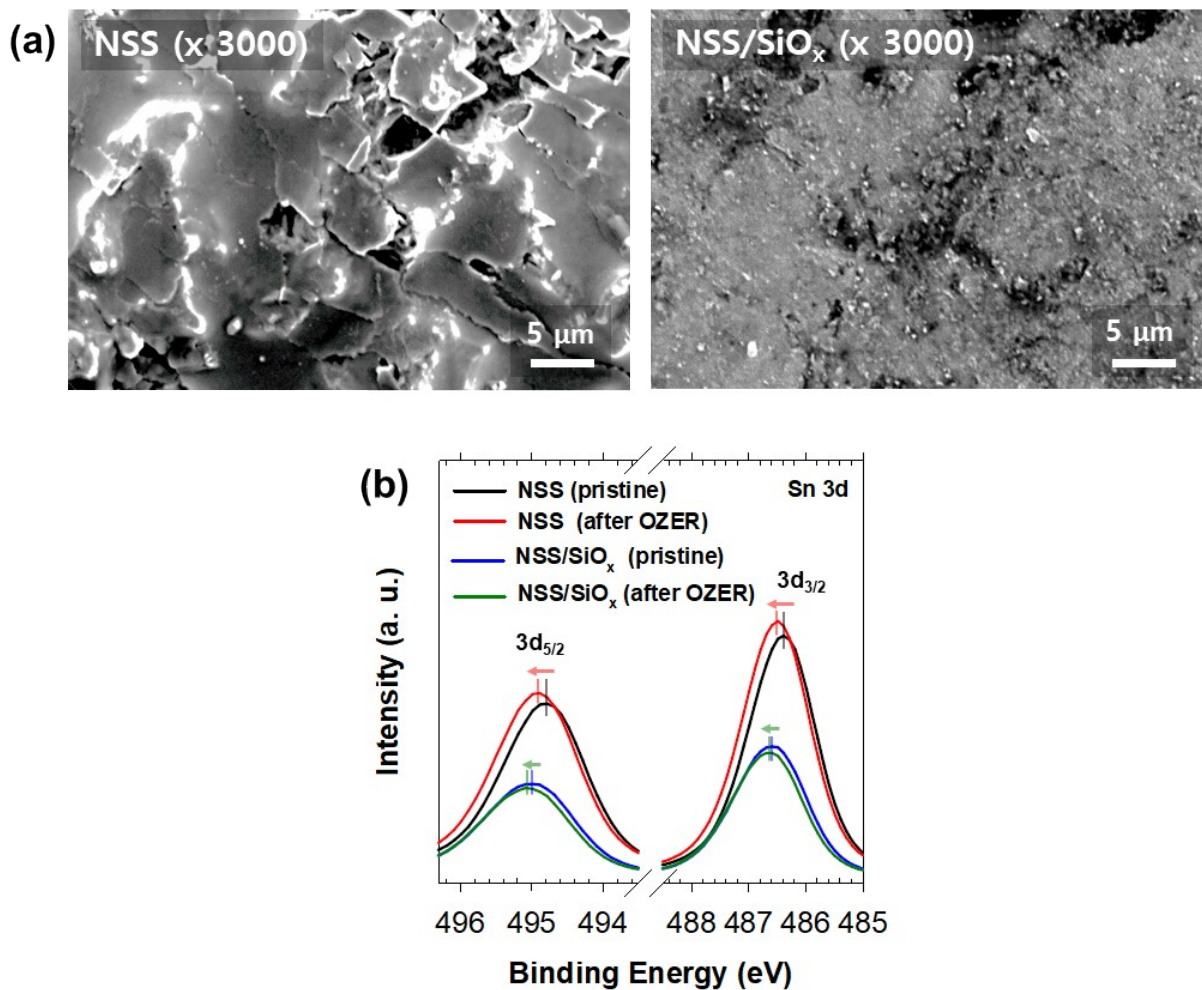
Fig. S4. (a) SEM images and (b) Sn 3d XPS spectra for NSS and NSS/SiOx after the OZER ($t = 4$ hours, $j = 10$ mA cm^{-2}, electrolyte = 0.5 M H_2SO_4)

Table S1. Dissoluted metal ions from the catalysts after the OZER ($t = 4$ hours, $j = 10$ mA cm^{-2}, electrolyte = 0.5 M H_2SO_4)

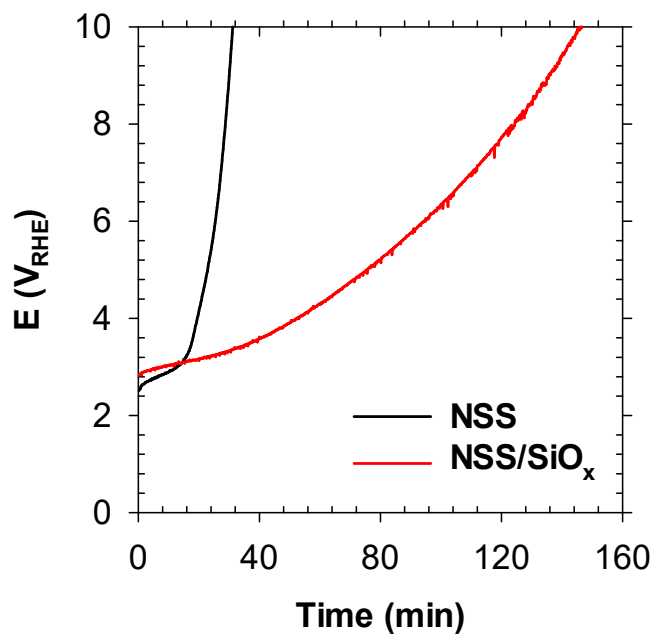| Post-OZER sample	Ni (μM)	Sn (μM)	Sb (μM)
NSS	1.72	2.21	1.36
NSS/SiO$_x$	0.43	0.28	0.11

Fig. S5. The evolution of cell potential for NSS and NSS/SiO$_x$ anodes in accelerated life tests at j = 100 mA cm$^{-2}_{geo}$ in the 0.5 M H$_2$SO$_4$ solution.

3. Potential of zero charge (PZC) determination

The PZC was determined in a three-electrode cell (without gas purging) based on the potential reaching a local minimum of capacitance (F), as shown in Fig. S6.[13] The capacitance under varying potentials was monitored by electrochemical impedance spectroscopy programmed in a potentiostat (VSP, BioLogic). The impedance spectra, as functions of the applied potential, were recorded in 0.05 M H$_2$SO$_4$ solutions at a frequency of 150 mHz and sinus amplitude of 5 mV. After fitting the spectra to 6th-order polynomials ($R^2 > 0.9978$), the potential value at the minimum F was defined as the PZC.
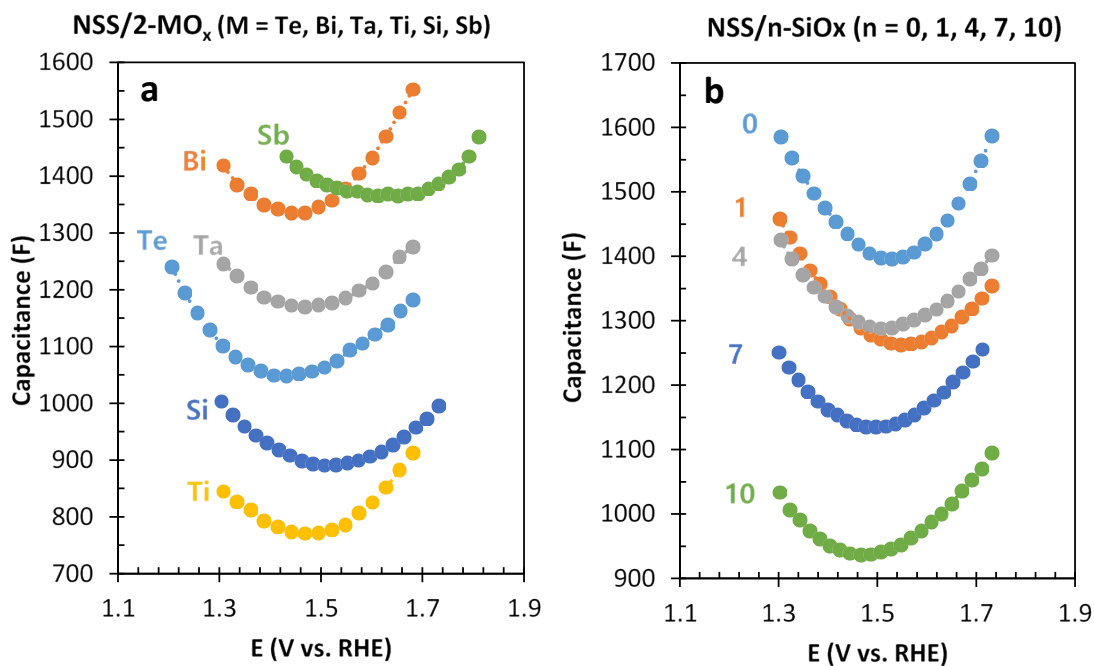
Fig. S6. Evolutions of capacitance as functions of applied anodic potential (E) for NSS/n-SiO$_x$ with variable (a) M (Sb, Bi, Ta, Te, Si, and Ti) and (b) n for SiO$_x$ (0 to 10); electrolyte = 0.05 M H$_2$SO$_4$, frequency = 150 mHz, sinus amplitude = 5 mV, drift-corrected. Each spectrum was fitted to 6th-order polynomial to estimate the potential of zero charge.

4. Scanning electrochemical microscopy (SECM) analysis

The OZER overpotential (η_{OZER}) was determined using SECM enabling a precise electrochemical analysis with reduced effects of *iR*-drop and double layer charging current.[14] All SECM experiments were conducted in a bipotentiostat workstation (M470, BioLogic). The substrate samples were taped to have a geometric surface area of 0.28 cm^2_{geo}. A Pt ultramicroelectrode (UME) tip (BioLogic) with 10 µm diameter and RG ratio (radius of the glass sheath/radius of UME) of 10 was employed for the dissolved O_3 detection. The Pt UME tip was stabilized in 5 mM $K_3Fe(CN)_6$ + 100 mM KCl solutions until reproducible cyclic voltammograms were obtained (Fig. S7a). Sequentially, a distance between the tip and substrate (*d*) was estimated from the approach curve, fitted to a theoretical model as shown in Fig. S7b.[15]
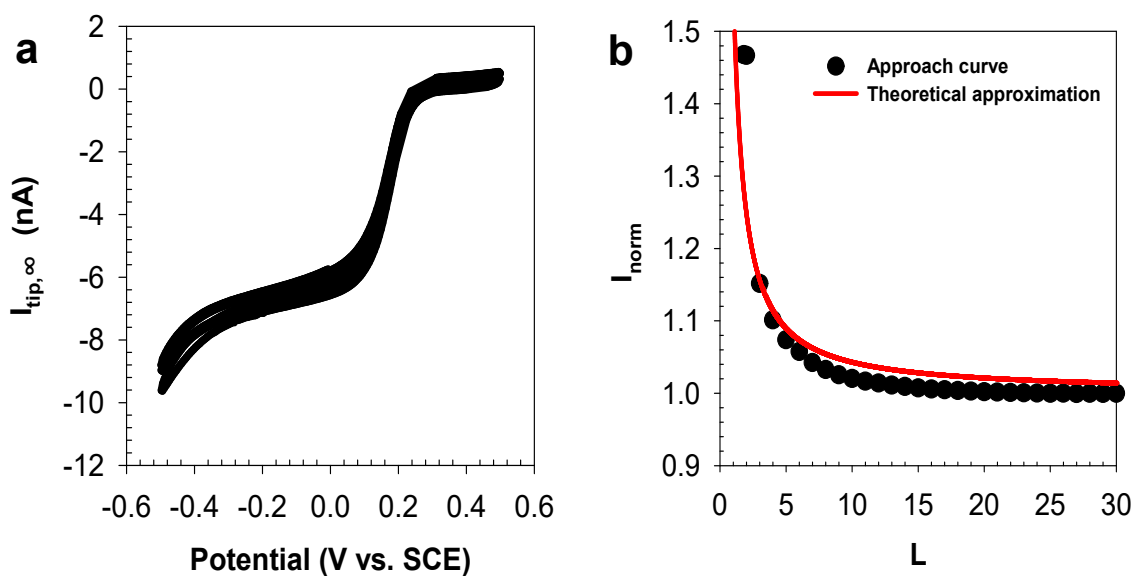

Fig. S7. (a) CVs during the stabilization of Pt UME tip (scan rate = 50 mV s⁻¹) in bulk and (b) normalized approach curve for determining *d* (step size of 5 µm and approach velocity of 1 µm/s). The $I_{tip,\infty}$ and I_{norm} indicate the tip current in bulk (far enough from the sample to be free from the feedback) and the normalized tip current ($I_T/I_{T,\infty}$), respectively. The *L* denotes *d/a*, where *a* is the Pt UME tip radius (5 µm). The electrolyte was 5 mM $K_3Fe(CN)_6$ mixed with 100 mM KCl.

A sample generation/tip collection (SG/TC) mode of SECM was employed to determine the onset potential (E_{on}) of OZER. As shown in Fig. S8a, the potential of ozone reduction reaction (OZRR) at the tip was discriminated based on cyclic voltammetry (CV) in O_2 saturated solutions, with and without dissolved O_3 produced by a pre-anodization (10 mA cm^{-2} for 10 min) of the NSS/2-SiO$_x$ sample. The E_{on} values of oxygen reduction reaction (ORR) and OZRR were estimated to be 0.6 V and 1.35 V$_{Ag/AgCl}$, respectively. Accordingly, the tip potential of 0.7 V$_{Ag/AgCl}$ was chosen as the tip potential for a selective OZRR. To fix the d at ~260 μm, the approach curve was generated for each sample in the ferricyanide electrolytes. Subsequently, the electrolyte was replaced with 0.5 M H_2SO_4 solution for the detection of the OZER E_{on}. A stepwise potential increase (10 mV every 5 min) was applied to the O_3 generating substrate, while the OZRR current at the UME tip (I_{tip}) was monitored, as presented in Fig. S8b. The OZER E_{on} was determined when the absolute value of I_{tip} reached 1 nA. Finally, the η_{OZER} was calculated by the following equation:

$$\eta_{OZER} = E_{on, \, OZER} - (E°_{OZER} - 0.059 \cdot pH) \tag{S1}$$

where $E_{on, \, OZER}$ is the OZER onset potential vs. Ag/AgCl, $E°_{OZER}$ is the standard.

The homogeneity of the local OZER activity on the sample surface was interrogated by SECM areal scan shown in Fig. S9. The result indicates that there was an insignificant local variance of the OZER activity among the catalyst surface, while a distinct difference between samples was observed, corroborating the validity of the OZER overpotential measurement on a random point.
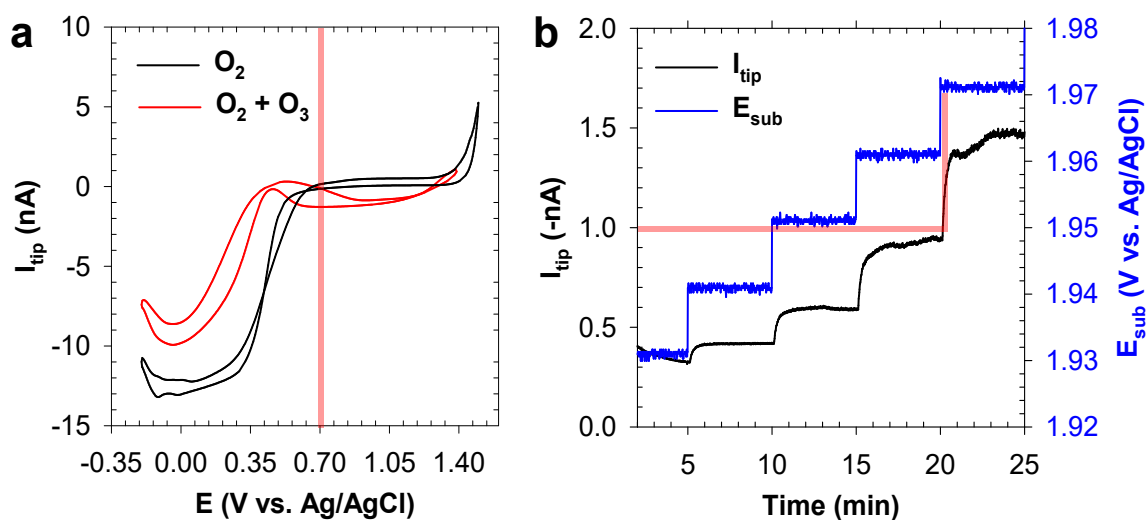
Fig. S8. (a) CVs for Pt UME tip (scan rate = 50 mV s^{-1}) in bulk with and without dissolved O_3 (in saturated O_2) and (b) chronoamperometry (CA) of the Pt UME tip upon a stepwise increase of potential (by 10 mV for 5 min in each step) on the NSS where the $E_{on, OZER}$ was determined to be 1.97 $V_{Ag/AgCl}$ at the I_{tip} basis of 1 nA. The electrolyte was 0.5 M H_2SO_4.
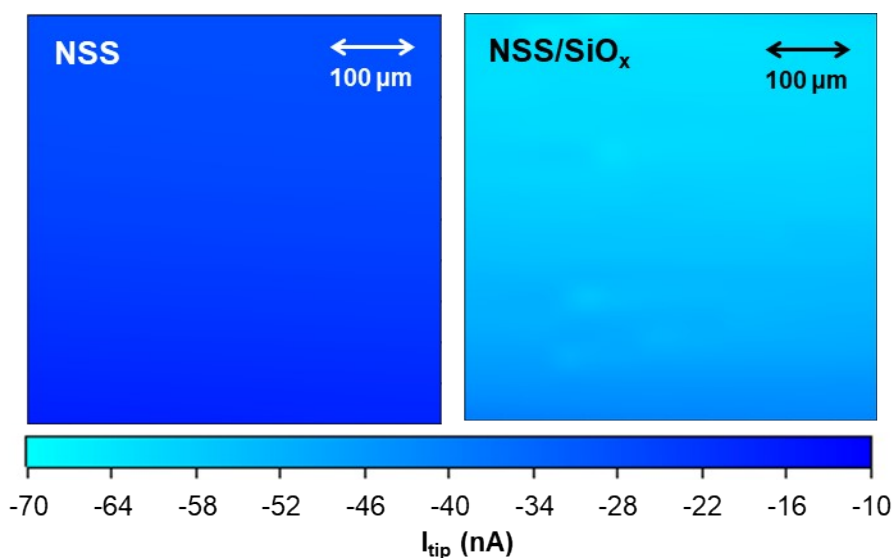

Fig. S9. The SECM areal scan images of the OZER activity for the NSS and NSS/SiO$_x$ anodes (step size = 25 μm point^{-1}, scan velocity = 250 μm s^{-1}, d = 100 μm, E_{sub} = 2.2 V_{RHE}, E_{tip} = 0.62 V_{RHE}, electrolye = 0.5 M H_2SO_4).

The E_{on} of OER was also determined in the SECM apparatus for NSS/MO$_x$ (M = Te, Bi, Ta, Ti, Si, and Sb), based on the potential at j of 0.1 mA cm^{-2}$_{geo}$ (geometric surface area = 0.28 cm^2$_{geo}$) from the linear sweep voltammetry (LSV) at scan rate of 25 mV s^{-1} in 0.5 M of H$_2$SO$_4$ (saturated with O$_2$). The OER overpotential (η_{OER}) was calculated by the following equation:

$$\eta_{OER} = E_{on, OER} - (E°_{OER} - 0.059 \cdot pH) \tag{S2}$$

where $E_{on, OER}$ is the OER onset potential vs. Ag/AgCl at j of 0.1 mA cm^{-2}$_{geo}$, $E°_{OER}$ is the standard potential for OER (1.02 V$_{Ag/AgCl}$ or 1.23 V$_{SHE}$) and the measured pH was 0.3 for 0.5 M H$_2$SO$_4$ solutions. The η_{OER} values were plotted versus the PZC in Fig. S10a. Additionally, the η_{OZER} was plotted in relation with two different types of electronegativity of the overcoated metal oxides: i) ionic electronegativity[16] and ii) grouped electronegativity in Allen scale[17] (Fig. S10b and c, respectively). The outer metal oxides were assumed to have the same oxidation state as precursors. In Fig. S10b, the overall linear relation between ionic electronegativity and PZC was revealed, while the Bi^{3+} deviated from the trend. In contrast, higher valency of Bi (Bi^{5+}) was compatible with the trend, suggesting the Bi component could be further oxidized during annealing. The grouped electronegativity was calculated as follows.[18] For example, the value of SiO$_x$ was 2.92 by assuming SiO$_2$ [(1.916 for Si) × (3.61 for O)^2]$^{1/3}$.

In Fig. 3, the sensitivity of CE to the varying PZC was found to be much greater than that of η_{OZER}; NSS/TeO$_x$ and NSS/SbO$_x$ located in both ends gave only 3.3 and 2.9% of CE, respectively. In addition, the activity trend in Fig. 3a was incompletely matched with the selectivity trend in Fig. 3b. These discrepancies could be justified by the fundamental differences between thermodynamic and kinetic parameters. In other words, the CE of OZER would be collectively influenced by η_{OZER},

η_{OER}, and the charge transfer coefficients of OER and OZER. In comparison, the η_{OZER} would be relatively independent on the side reaction and the kinetic parameters.
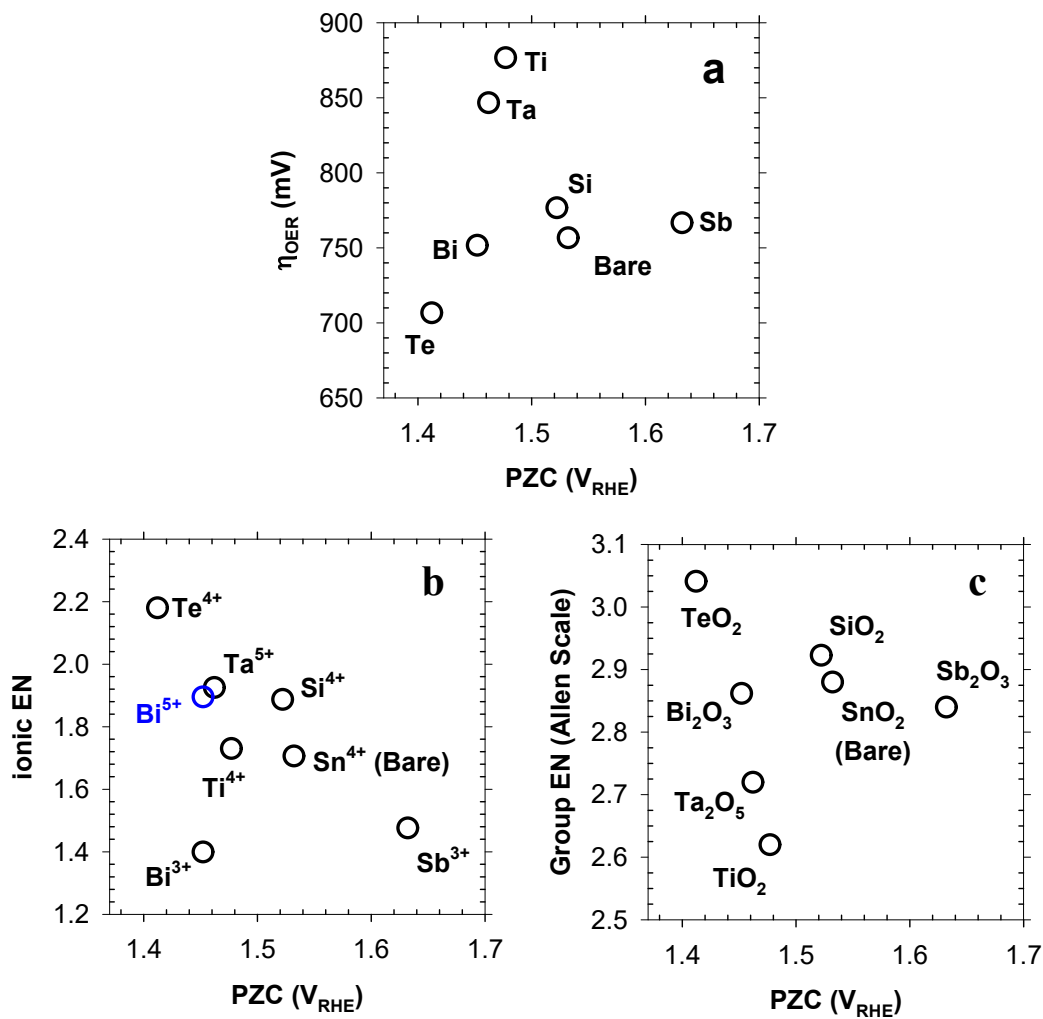

Fig. S10. Correlations of PZC with (a) η_{OER}, (b) group electronegativity (EN), and (c) ionic EN for the NSS/2-MO_x (M = Te, Bi, Ta, Ti, Si, and Sb). The η_{OER} was determined in the SECM apparatus.

5. Determination of the specific OER activity

The specific OER activity was compared based on LSV with *iR*-compensation for the applied potential and normalization of *j* by ECSA. The ECSA was estimated from the double-layer capacitance and calculated by the following equation:

$$ECSA = C_d/C_s \tag{15}$$

where C_d is the double-layer capacitance, and C_s is the specific capacitance (0.035 mF/cm^2 in the H$_2$SO$_4$ electrolyte for metal oxides).[18, 19] Cyclic voltammetry at various scan rates (0.005, 0.01, 0.025, 0.05, 0.1, 0.2, 0.4, and 0.8 V s^{-1}) was employed in the non-Faradaic region ($\pm$200 mV potential window from open-circuit potential (OCP)), as shown in Fig. S11a. The working electrode was held at OCP for 30 s before changing the scan rate. The non-Faradic currents at 0.6 V$_{Ag/AgCl}$ were sampled for each scan rate, to be plotted against the scan rate (Fig. S11b). The linear slopes corresponded to C_d based on the average of the absolute values for the anodic and cathodic currents. Consequently, the ECSA values of NSS/n-SiO$_x$ anodes are illustrated in Fig. S12.
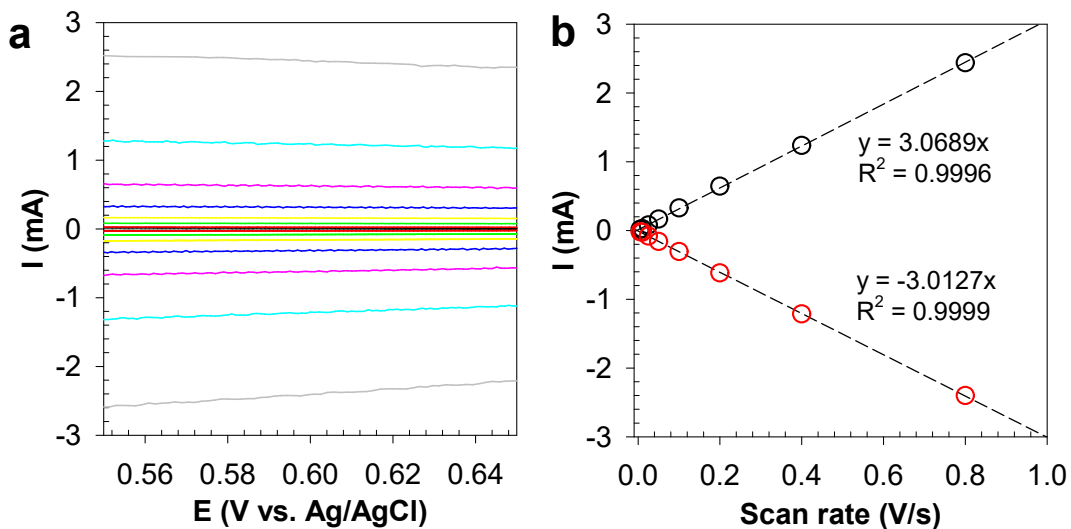
Fig. S11. Representative ECSA determination for NSS based on (a) CVs in the non-faradaic region in 0.5 M H_2SO_4 (with scan rate of 0.005, 0.01, 0.025, 0.05, 0.1, 0.2, 0.4, and 0.8 V s^{-1}) and (b) the anodic/cathodic currents at 0.6 $V_{Ag/AgCl}$ as functions of scan rates. The average values of the anodic/cathodic slopes were used for the ECSA determination.
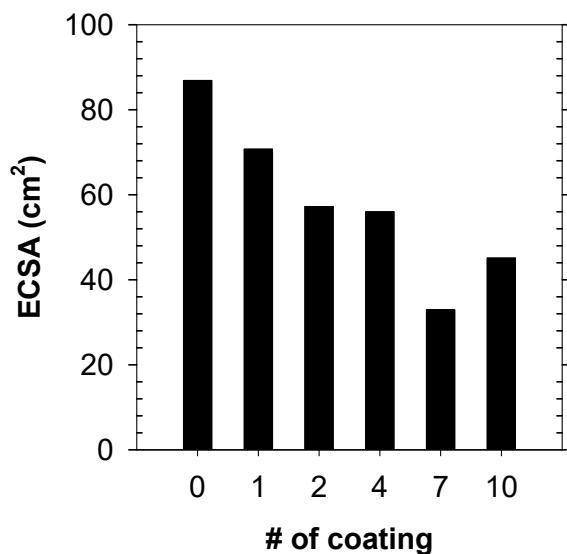

Fig. S12. The estimated ECSA of NSS/n-SiO$_X$ for variable n (0, 1, 2, 4, 7, and 10).

To exclude the influence of the roughness factor (i.e., number of active sites), the LSV curves were normalized by ECSA. The iR drop was compensated at the 85% level, based on a current interruption (CI) method using the EC-Lab software (Biologic).[20] The measured uncompensated resistances (R_u) of the NSS/n-SiO$_x$ electrodes are summarized in Table S2. The OER overpotential from the specific current density was determined by the following equation:

$$\eta_{OER} = E_{on,\ OER} - (E°_{OER} - 0.059 \cdot pH) \tag{16}$$

where η_{OER} is the OER overpotential at 0.5 mA cm$^{-2}_{ECSA}$, $E_{on,\ OER}$ is the OER onset potential at 0.5 mA cm$^{-2}_{ECSA}$, and $E°_{OER}$ is the standard reduction potential for OER, which equals 1.23 V$_{SHE}$; the pH was 0.3 for the 0.5 M H$_2$SO$_4$.

Table S2. The solution, film, and charge resistances (R_s, R_f, and R_{ct}), derived from the Nyquist plots and equivalent circuit (Fig. 2b), in comparison with the uncompensated resistances (R_u) by the CI method and the oxygen evolution reaction (OER) overpotential at 0.5 mA cm$^{-2}_{ECSA}$ (Fig. 2a).

number of coatings (n)	R_s (Ω)	R_f (Ω)	R_{ct} (Ω)	R_u (Ω) (by CI method)	η_{OER} (V) (at 0.5 mA cm$^{-2}_{ECSA}$)
0	0.38	1.7	20	0.5	1.03
1	0.40	0.2	22	0.6	1.06
2	0.41	0.8	28	1.0	1.07
4	0.41	8.1	61	2.5	1.15
7	0.36	16	53	3.4	1.14
10	0.41	11	48	2.8	1.13

6. Determination of Nyquist plots for OER

The OER on NSS/n-SiO$_x$ anodes was further explored in terms of Nyquist plots over the frequency range from 100 mHz to 100 kHz, and sinus amplitude of 10 mV in 0.5 M H$_2$SO$_4$ solutions. The anodic potential of 2.18 V$_{NHE}$, (below the O$_3$ on-set potential) was the baseline potential during the impedance analysis. The obtained Nyquist plots were fitted to an equivalent circuit shown in Fig. 2b(inset), and the derived resistances are summarized in Table S2.

7. Material characterization

The horizontal and cross-sectional morphologies were observed by a high-resolution field-emission scanning electron microscope (FE-SEM, JSM 7800F PRIME, JEOL) in Fig. S13. The depth profiles of the element compositions were investigated by GDS (850A, LECO) in Fig. S14. The X-ray diffraction (XRD) patterns were monitored at 2θ of 20°–80° with a 0.02° step size, at 40 kV and 15 mA, using an X-ray diffractometer (MiniFlex 600, Rigaku) in Fig. S15a. The functional groups on the catalyst surfaces were analyzed by attenuated total reflection-Fourier-transform infrared spectroscopy (ATR-FTIR; Scientific iS50, Thermo Fisher Scientific) using the ZeSe crystal. The atomic compositions and oxidation states of the atoms on the catalyst surfaces were explored by XPS (K-ALPHA XPS system, Thermo Fisher Scientific) using a monochromated Al Kα irradiation source (12 kV, 72 W, 1486.6 eV, 400 μm spot size). The binding energy positions in the XPS spectra were calibrated with regard to the location of the C 1s peak (284.6 eV). The X-ray absorption near edge structure (XANES) and extended X-ray absorption fine structure (EXAFS) spectra of Sn K-edge were collected in the fluorescence mode at 10C Beamline of Pohang Accelerator Laboratory (PAL), as shown in Fig. S16 and S12b, respectively. The beam from the synchrotron radiation source was monochromatized by a Si (111) monochromator during the measurements, and the beam intensity was detuned by 20% in order to avoid unwanted higher harmonics.
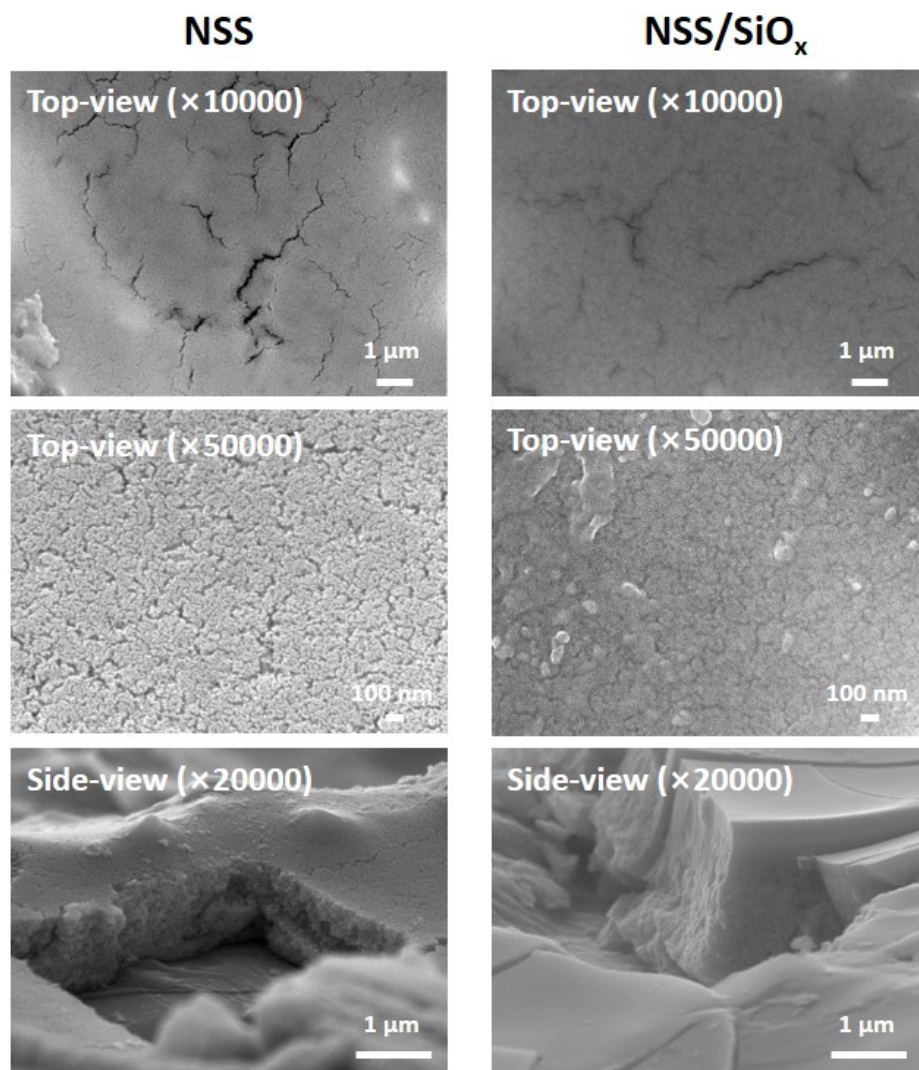
Fig. S13. Representative horizontal (10 and 50 k magnification) and cross-sectional (20 k magnification) SEM images of the NSS and NSS/SiO$_x$ anodes.
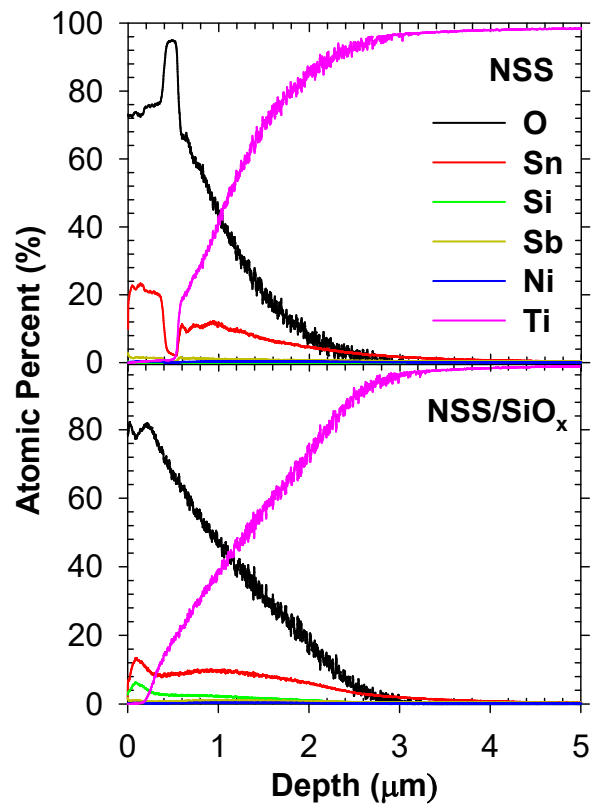
Fig. S14. Depth profiles of atomic ratios for NSS and NSS/SiO$_x$, measured by GDS (Depth 0 corresponds to the surface). The Sn and Si profiles roughly estimate the thickness of the catalysts layer and mixing level between NSS and SiO$_x$.
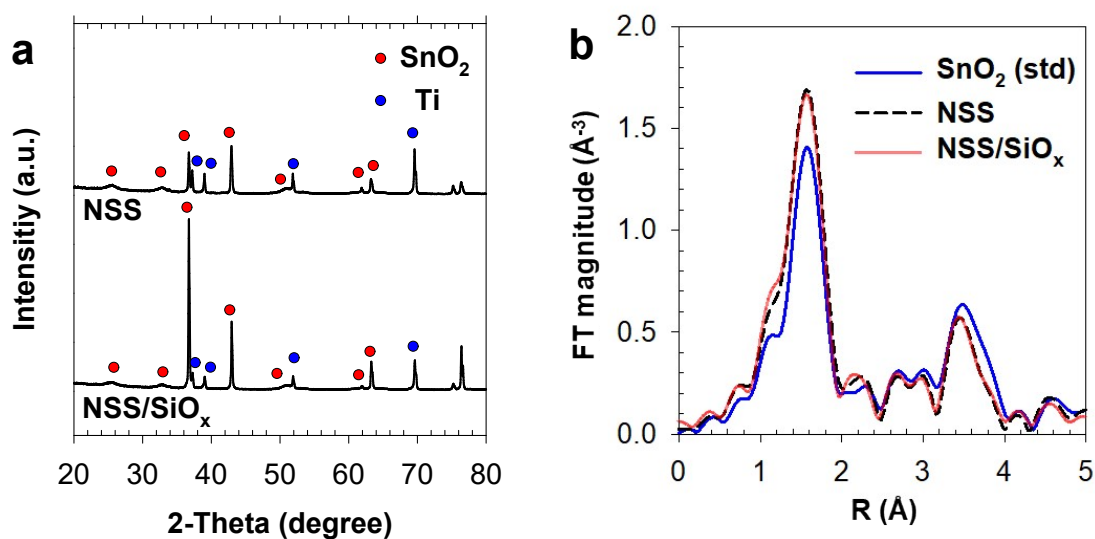
Fig. S15. (a) XRD patterns and (b) Sn-*K* edge EXAFS spectra (k^3-weighted) of NSS and NSS/SiO$_x$ anodes. The reflections in the XRD patterns at 26.7°, 34.0°, 38.0°, 43.5°, 51.9°, 54.8°, 64.6°, and 66.1° correspond to SnO$_2$ crystal planes of (110), (101), (200), (210), (211), (112), and (301), respectively (JCPDS 41-1445).[21] The Ti metal peaks (JCPDS 44-1294) from the substrate were also noted. The peaks in the EXAFS spectra located at 1–2 Å and 2.5–4 Å indicate Sn–O and Sn–Sn bonds of the rutile SnO$_2$ structure, respectively.[22] The standard SnO$_2$ powder sample was also compared as a reference.
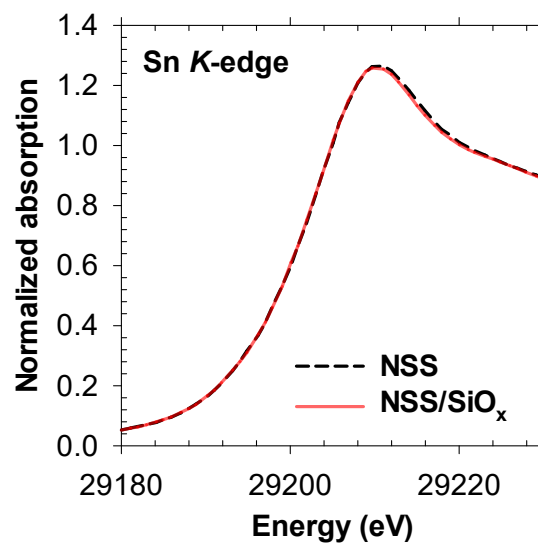
Fig. S16. Normalized Sn K-edge XANES spectra of NSS and NSS/SiO$_x$ anodes.

Table S3. Relative elemental composition on the surface of NSS and NSS/SiO$_x$ (depicted in Fig. 4a).

Element	NSS (at. %)		NSS/SiO$_x$ (at. %)	
	Total	Sn-based	Total	Sn-based
O	63.9	-	63.7	-
Si	0.0	0	20.0	126
Sn	34.1	100	15.9	100
Sb	1.2	3.7	0.2	1.4
Ni	0.6	1.7	0.2	1.1
Ti	0.2	-	0.0	-

8. OZER under various conditions

To clarify the OZER mechanism, the electrolysis was performed under various conditions. First, the influences of variable dissolved oxygen concentrations in electrolytes were interrogated. In a control electrolyte open to the atmosphere, the dissolved oxygen concentration was ~8 mg L^{-1}. Argon gas was purged into the electrolyte to give a negligible amount of dissolved oxygen, whereas oxygen gas was bubbled to obtain a saturated condition (> 30 mgO$_2$ L^{-1}). In addition, 0.1 M of *tert*-butanol was added as an •OH quencher. Fig. S17 shows that the gas purging or the scavenger addition led to negligible variation in the OZER. Therefore, as described in the main manuscript, the electrochemical ozone generation mechanism primarily involving the free dissolved O$_2$ and •OH could be ruled out.
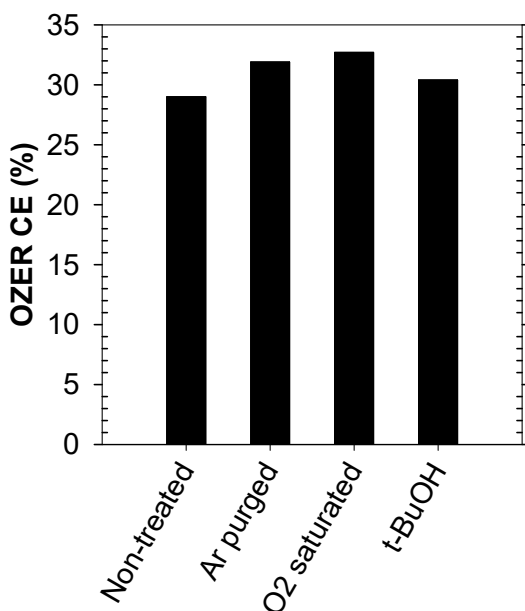

Fig. S17. The OZER current efficiency in galvanostatic electrolysis (calculated for initial 3 minutes of reaction) with and without gas (Ar, O$_2$) purging and scavenger (*t*-BuOH) addition; anode = NSS/2-SiO$_x$, electrolyte = 0.5 M H$_2$SO$_4$, counter electrode = Pt, reference electrode = Ag/AgCl (3 M AgCl), j = 10 mA cm$^{-2}_{geo}$.

9. Theoretical analysis

The theoretical calculations were performed in a density functional theory (DFT) framework with the plane-wave technique, as implemented in the Vienna ab-initio Simulation Package.[23] The Perdew–Burke–Ernzerh of generalized gradient approximation functional was used to describe the exchange-correlation energy.[24] The effect of the core electrons on the valence electron density was represented using the projector augmented wave method. A kinetic energy cutoff of 400 eV was employed for the expansion of the plane wave. Additionally, all atoms were relaxed using a conjugate gradient algorithm until the forces on all unrestricted atoms were <0.03 eV Å^{-1}. All calculations were performed considering spin polarization.

The OZER was evaluated in two systems: (1) NSS and (2) NSS/SiO$_x$. First, the (2 x 2) unit cell (6.48 Å × 6.83 Å) slab model of the most stable rutile (110) SnO$_2$ was constructed and optimized.[25] Thereafter, two surface Sn atoms were substituted with Ni and Sb atoms after testing all possible doping configurations, and the final surface structure is illustrated in Fig. S20a and b, which are consistent with the results of Gibson *et al.*.[26] The NSS/SiO$_x$ model was constructed as the (2 x 2) unit cell (5.95 Å × 6.49 Å) slab model of the completely mixed rutile NSS/SiO$_x$ (110) structure, as shown in Fig. S20c and d. It has been established that the SiO$_x$ could thermally diffuse into the lattice without changing the host oxide.[27-29] In addition, we have experimentally substantiated the mixed structure based on the following pieces of characterization evidence: (i) In the XPS spectra, the Sn 3d and Sb 3d peaks of NSS (Fig. 4c and d) exhibited a positive shift, attributed to the SiO$_x$ heterojunction, which indicated the strong chemical interactions between NSS and SiO$_x$. (ii) The surface atomic compositions based on XPS (Fig. 4a) showed that approximately half of the surface Sn was substituted by Si with marginal change in the oxygen fraction after the coating. (iii) The Sn–O–Si peaks in the FTIR spectra (Fig. 4b) and GDS depth

profiles (Fig. S14) clearly indicate the thermal inter-diffusion between SiO_x and NSS. (iv) XRD patterns and EXAFS spectra (Fig. S15a and b, respectively) indicate that the rutile structure of NSS was preserved by the SiO_x overcoating, which implies the negligible segregation into SiO_x (at least on the surface).

A Monkhorst–Pack grid of $4 \times 4 \times 1$ *k*-point meshes was sampled using the Methfessel–Paxton integration scheme for both surface models.[30] Approximately 12 Å thick slabs of four layers, with the bottom two layers fixed and the top two layers relaxed, were employed. Vacuum (15 Å) was applied along the z-direction for both models to avoid lateral interactions. The activation energies were calculated using the CI-NEB method.[31] The transition state configurations and minimum energy pathways were optimized using 3–5e intermediate images, until the maximum atomic forces converged to less than 0.05 eV/Å. Furthermore, we carefully examined the surface model with an oxygen vacancy on the bridge site, as proposed by Gibson *et al.*.[26] We found that the O* intermediate preferred to be adsorbed on the vacant bridge site over other adsorption sites, restoring the bridge oxygen. However, the two important steps, the O_2*- and O_3*-formation steps, were thermodynamically evaded on the vacancy model. The O_3*-formation step (binding of O_2* and O*) required 2.31 and 2.90 eV of endothermicity for NSS and NSS/SiO_x, respectively, when the surface possessed one oxygen vacancy. In contrast, the reaction was slightly endothermic on pristine NSS and exothermic on pristine NSS/SiO_x without the oxygen vacancy. The O_2*-formation step (binding of two O* atoms) also presented 0.30 and 0.11 eV endothermicity values, respectively, on the one-vacancy NSS and NSS/SiO_x model, whereas the reaction was exothermic on the pristine surface. These results indicate that the OZER occurred by the combination of formed O* atoms, as proposed in Fig. 5b and c, not using the bridge oxygen, which leads to an O vacancy.

The ΔG was calculated using the computational hydrogen electrode model proposed by Nørskov *et al.*, as follows:[32]

$$\Delta G = \Delta E + \Delta ZPE - T\Delta S - neU \qquad (17)$$

where ΔE is the reaction energy obtained from the DFT calculations, ΔZPE is the DFT-calculated zero-point energy, S is the standard entropy obtained from NIST Chemistry WebBook,[33] coefficient n refers to the number of transferred electrons, U is the applied potential measured against RHE, and T is set to 298.15 K.

The adsorption energy (E_{ads}) was defined as follows:

$$E_{ads} = E_{mol/slab} - E_{slab} - E_{mol} \qquad (18)$$

where $E_{mol/slab}$ is the total energy of the adsorbates and the slab system, E_{slab} is the energy of the pristine slab, and E_{mol} is the energy of the DFT-calculated gas-phase molecule in a cubic unit cell of 15 Å. The optimized adsorption configurations and their E_{ads} values (or ΔG values) for OZER intermediates are depicted in Fig. S21 (for H_2O^*, O_2^*, and O_3^*) and Fig. S22 (for OH^*, O^*, and OOH^*). The atomic charge distributions of NSS and NSS/SiO_x were estimated by the Bader charge analysis (visualized in Fig. S23).[34] The values of the interfacial charge transfer between the electrode surface and adsorbed molecules were defined as the difference between the total number of electrons on the valence orbital of the molecule and the calculated occupancies of the same orbitals after adsorption.

In this study, the adsorption of O^* and O_3^* was classified as chemical bonding, whereas the adsorption of O_2^* was classified as physical bonding for the following reasons: i) the charge-transfer values of O^* and O_3^* were larger than 0.17 |e| (strong interaction), while that of O_2^* was less than 0.1 |e| (negligible interaction), as shown in Fig. 5d. ii) For O_3^*, a short M–O bond length with changed O–O bond lengths and vibrational frequency upon strong adsorption were observed

on both NSS and NSS/SiO$_x$ surfaces. Conversely, O$_2$* showed a long M–O bond and the unchanged O–O bond length even after adsorption, as illustrated in Fig. S24 and Table S4.
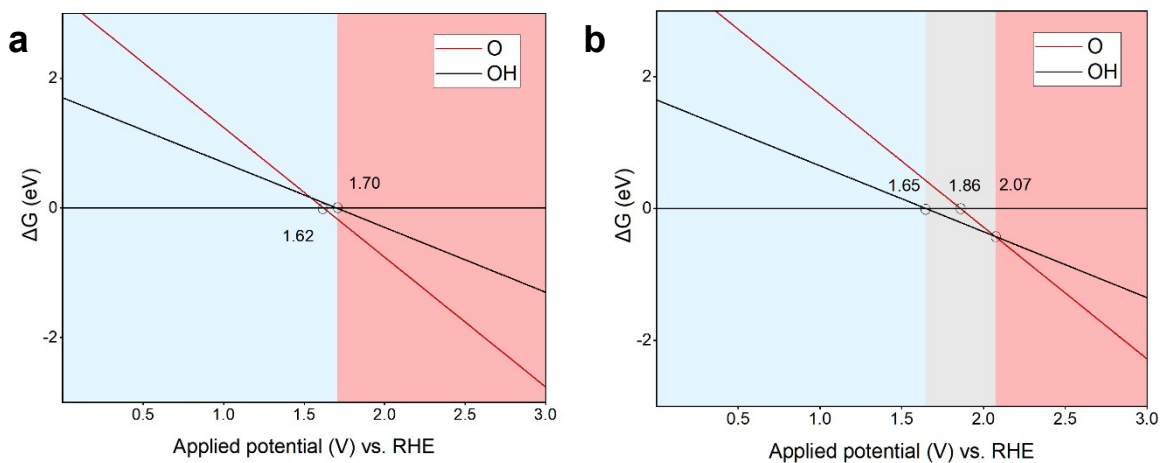

Fig. S18. Phase diagrams for the WOR intermediates on (a) NSS and (b) NSS/SiO$_x$ as a function of the applied anodic potential. The blue, gray, and red regions correspond to the H$_2$O*, OH* and O* dominating potential regions, respectively.
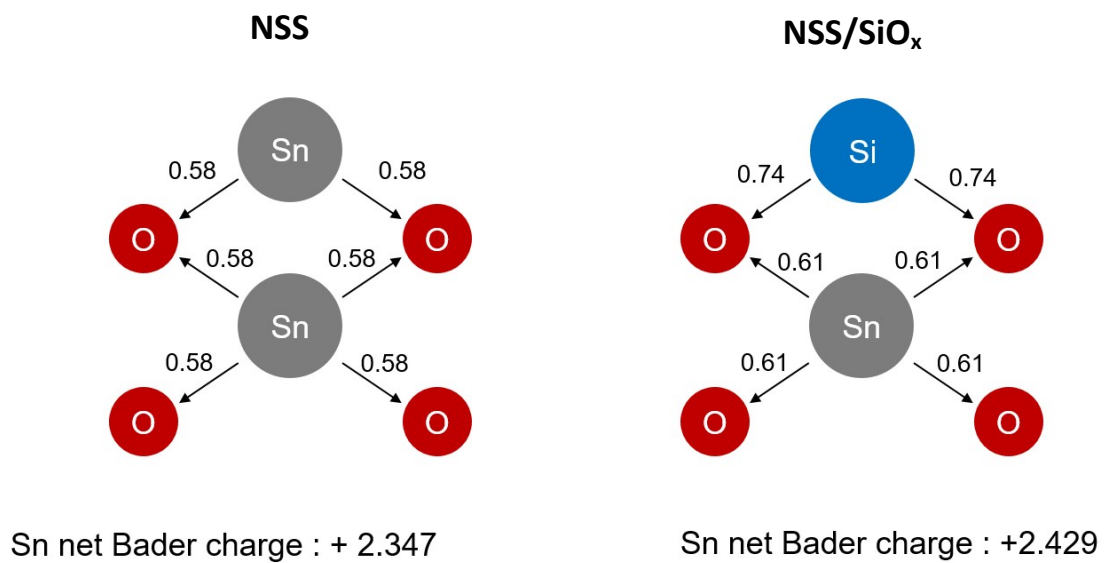
NSS

Sn net Bader charge : + 2.347

NSS/SiO$_x$

Sn net Bader charge : +2.429

Fig. S19. Schematic diagrams of charge transfer within intra-structures of NSS and NSS/SiO$_x$ (unit = |e|).
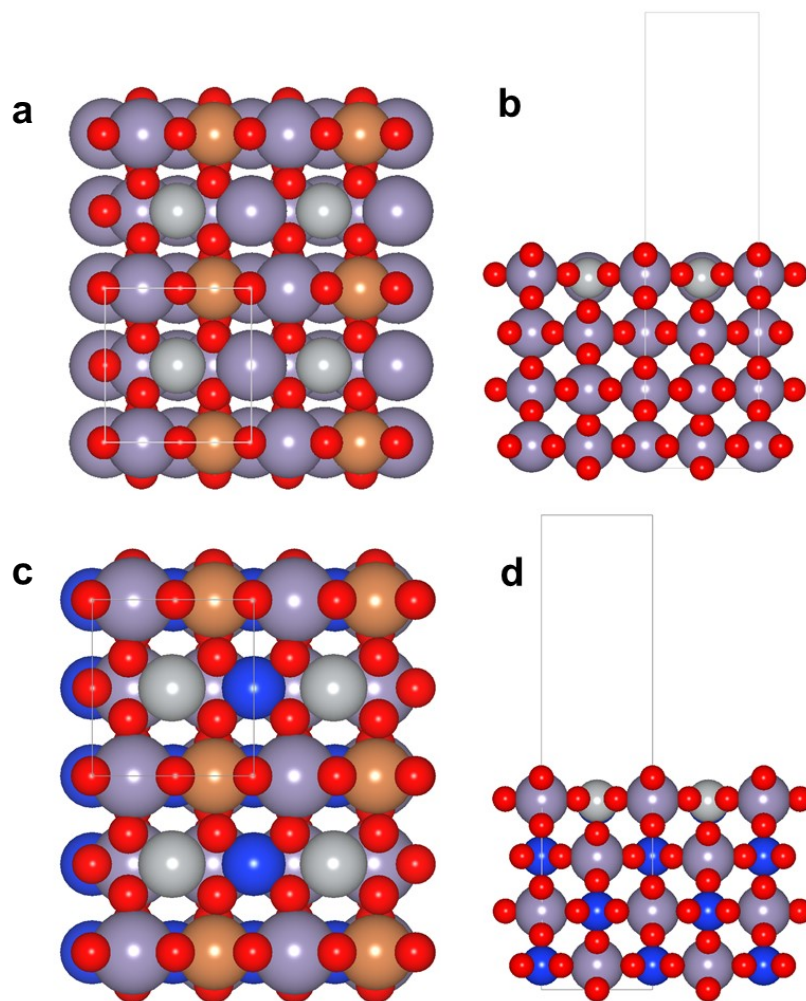
Fig. S20. (a, c) Top views and (b, d) side-views of DFT-optimized (a, b) NSS and (c, d) NSS/SiO$_x$. The blue, silver, red, purple, and orange balls represent Si, Ni, O, Sn and Sb atoms, respectively, while the gray box shows the unit cell.
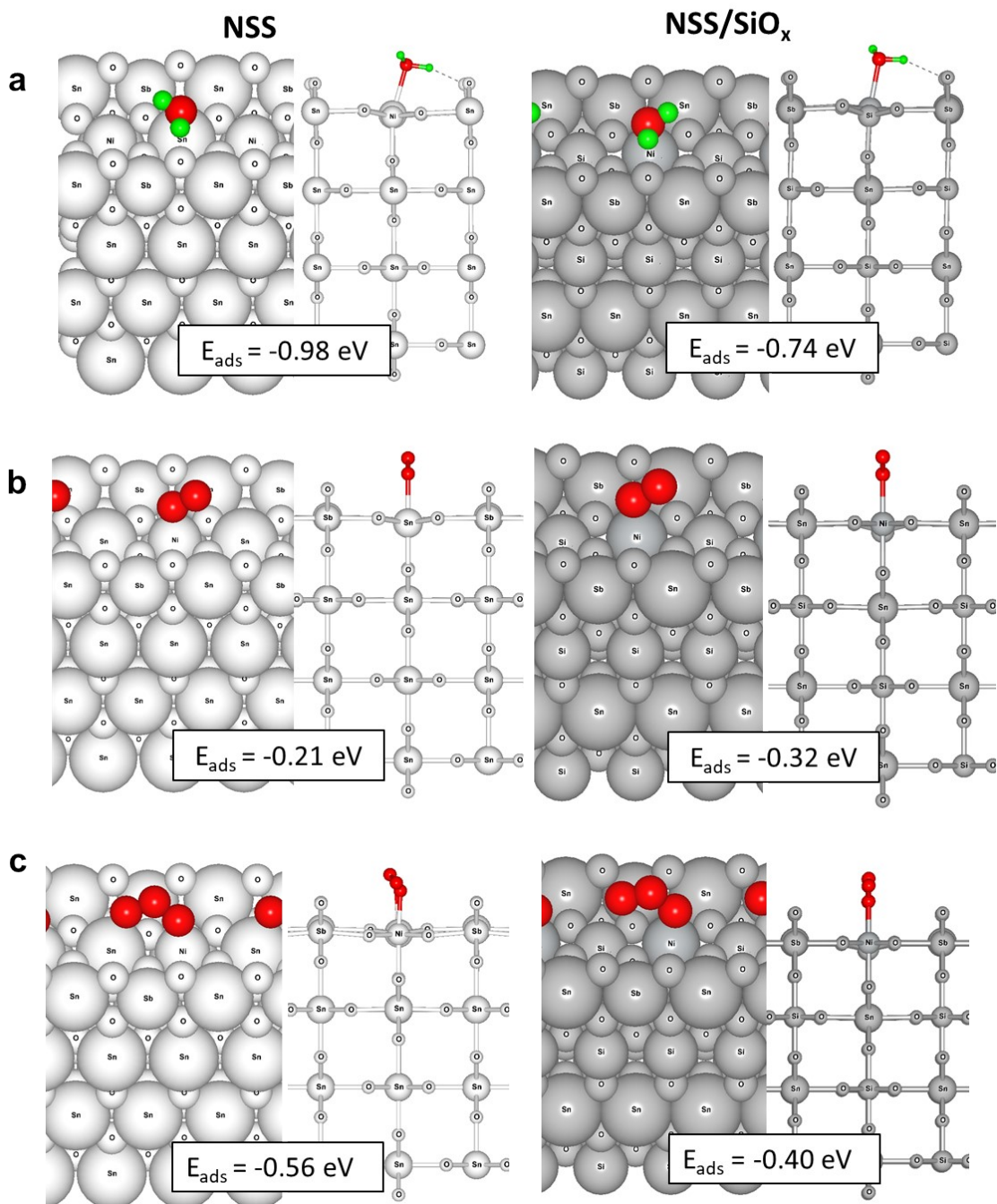
Fig. S21. DFT-optimized adsorption configurations and their adsorption energy values on NSS (white) and NSS/SiO$_x$ (grey) for (a) H$_2$O*, (b) O$_2$*, and (c) O$_3$*. The red and green balls represent the O intermediates and hydrogen atoms, respectively.
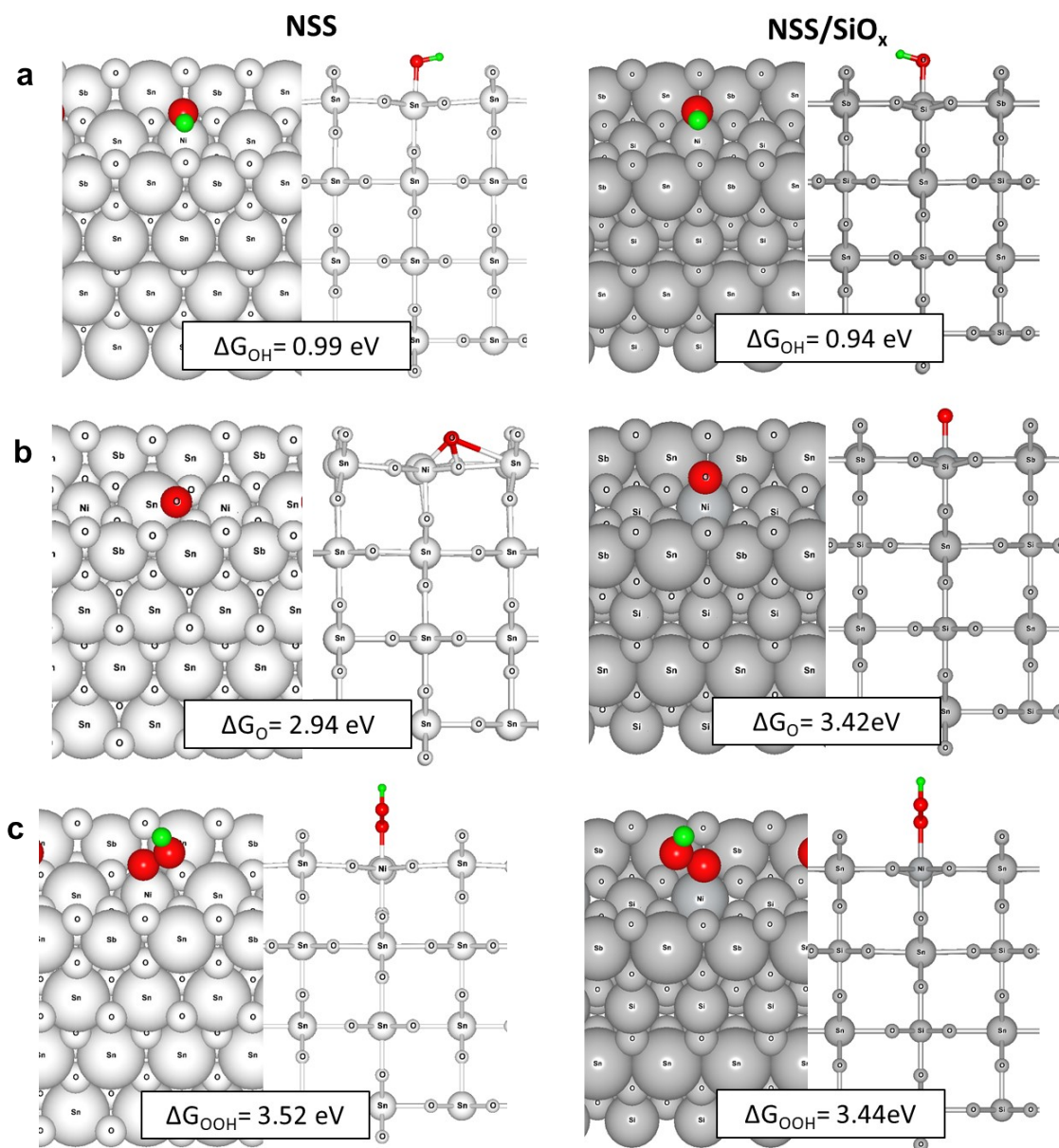
Fig. S22. DFT-optimized adsorption configurations and their free energy values on NSS (white) and NSS/SiO$_x$ (gray) at $U = 0.0$ V$_{RHE}$ for (a) OH*, (b) O*, and (C) OOH* intermediates. The red and green balls represent the O intermediates and hydrogen atoms, respectively.
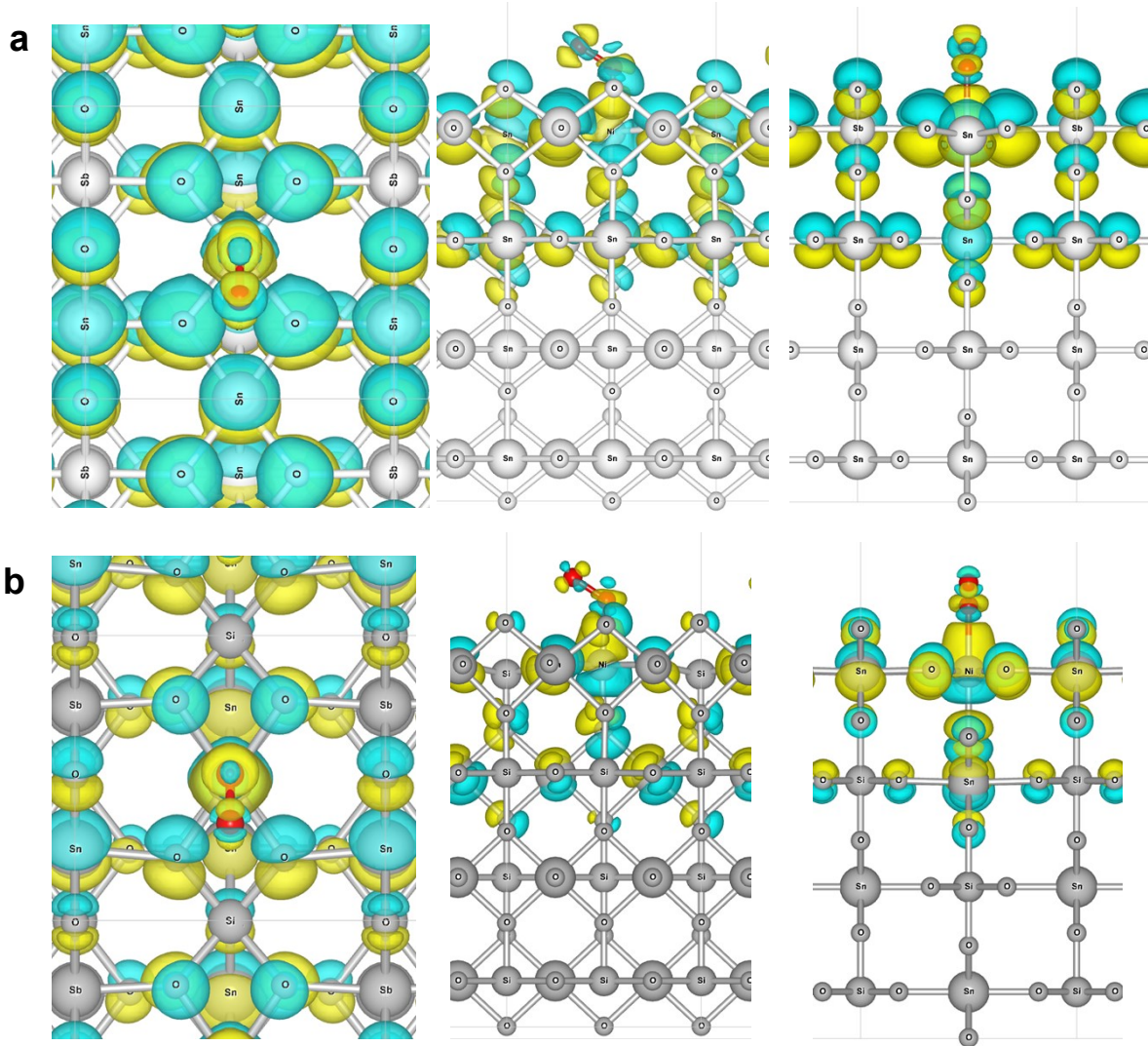
Fig. S23. Charge density distribution upon the adsorption of O₂* on (a) NSS and (b) NSS/SiOₓ with an iso-value of 0.005e Å⁻³. The red balls denote adsorbed oxygen molecules, while the gray balls indicate Sn, Si, Sb, and Ni atoms as labeled. The yellow and blue regions represent charge accumulation and depletion, respectively.
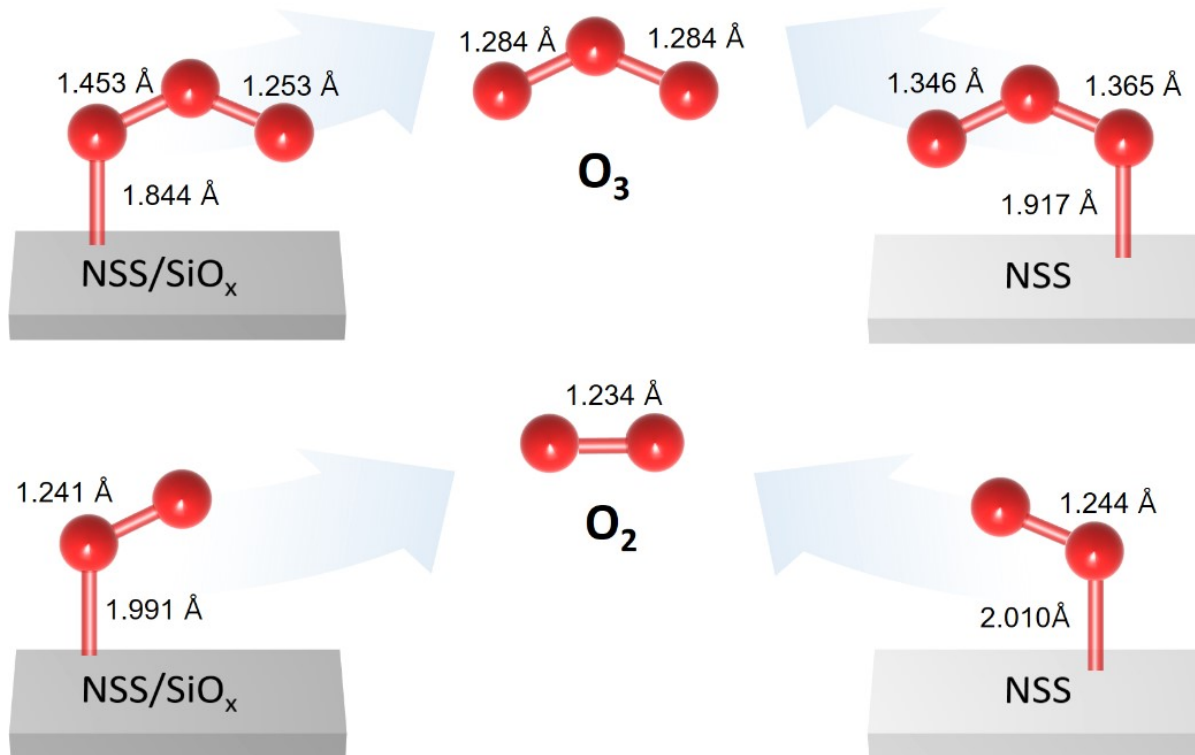
Fig. S24. A schematic representation of the bond length changes as either O_3 or O_2 was adsorbed on the surface of NSS and NSS/SiO$_x$.

Table S4. Bond length and stretching vibrational frequency of the surface O species. The M-O bond refers to the bond length between the catalyst and O intermediate, while the first/second O-O bonds refer to the bond length values between O intermediates.

| Catalyst | Intermediates | Bond length (Å) | | | Vibrational frequency ν (cm^{-1}) |
		d(M-O) (Å)	d(1st O-O) (Å)	d(2nd O-O) (Å)	ν(O-O) (cm^{-1})
Gas Phase	O_2		1.234		1566
	O_3		1.284	1.284	1284
NSS	O	1.466			
	O_2	2.010	1.244		1429
	O_3	1.917	1.365	1.346	980.0
NSS/SiO$_x$	O	1.682			
	O_2	1.991	1.241		1445
	O_3	1.844	1.453	1.253	1309

References

1. I. M. Abdullahi, J. Masud, P.-C. Ioannou, E. Ferentinos, P. Kyritsis and M. Nath, *Molecules*, 2021, **26**, 945.
2. K. Cho and M. R. Hoffmann, *Chemistry of Materials*, 2015, **27**, 2224-2233.
3. P. A. Christensen, K. Zakaria, H. Christensen and T. Yonar, *Journal of the Electrochemical Society*, 2013, **160**, H405-H413.
4. B. Correa-Lozano, C. Comninellis and A. De Battisti, *Journal of Applied Electrochemistry*, 1997, **27**, 970-974.
5. P. C. Foller and C. W. Tobias, *Journal of the Electrochemical Society*, 1982, **129**, 567.
6. L. Xu and J. Scantlebury, *Corros Sci*, 2003, **45**, 2729-2740.
7. D. Shao, W. Yan, X. Li, H. Yang and H. Xu, *Industrial & Engineering Chemistry Research*, 2014, **53**, 3898-3907.
8. D. Shao, X. Li, H. Xu and W. Yan, *RSC advances*, 2014, **4**, 21230-21237.
9. R. Kötz, S. Stucki and B. Carcer, *Journal of applied electrochemistry*, 1991, **21**, 14-20.
10. F. Montilla, E. Morallon, A. De Battisti, S. Barison, S. Daolio and J. Vazquez, *The Journal of Physical Chemistry B*, 2004, **108**, 15976-15981.
11. F. Vicent, E. Morallo, C. Quijada, J. Va, A. Aldaz and F. Cases, *Journal of applied electrochemistry*, 1998, **28**, 607-612.
12. J. Depasse and A. Watillon, *Journal of colloid and interface science*, 1970, **33**, 430-438.
13. L.-H. Shao, J. Biener, D. Kramer, R. N. Viswanath, T. F. Baumann, A. V. Hamza and J. Weissmüller, *Physical Chemistry Chemical Physics*, 2010, **12**, 7580-7587.
14. J. B. Allen and R. F. Larry, *Electrochemical methods fundamentals and applications*, John Wiley & Sons, 2001.
15. R. Cornut and C. Lefrou, *Journal of Electroanalytical Chemistry*, 2008, **621**, 178-184.
16. K. Li and D. Xue, *The Journal of Physical Chemistry A*, 2006, **110**, 11332-11337.
17. L. C. Allen, *Journal of the American Chemical Society*, 1989, **111**, 9003-9014.
18. C. E. Finke, S. T. Omelchenko, J. T. Jasper, M. F. Lichterman, C. G. Read, N. S. Lewis and M. R. Hoffmann, *Energy Environ Sci*, 2019, **12**, 358-365.
19. C. C. McCrory, S. Jung, I. M. Ferrer, S. M. Chatman, J. C. Peters and T. F. Jaramillo, *J Am Chem Soc*, 2015, **137**, 4347-4357.
20. R. Grief, R. Peat, L. Peter, D. Pletcher and J. Robinson, *Journal*, 1985.
21. K. S. Yoo, S. D. Han, H. G. Moon, S.-J. Yoon and C.-Y. Kang, *Sensors*, 2015, **15**, 15468-15477.
22. S. R. Davis, A. V. Chadwick and J. D. Wright, *The Journal of Physical Chemistry B*, 1997, **101**, 9901-9908.
23. G. Kresse and J. Furthmüller, *Physical review B*, 1996, **54**, 11169.
24. J. P. Perdew, K. Burke and M. Ernzerhof, *Physical review letters*, 1996, **77**, 3865.
25. M. Batzill and U. Diebold, *Progress in surface science*, 2005, **79**, 47-154.
26. G. Gibson, Z. Wang, C. Hardacre and W. F. Lin, *Phys Chem Chem Phys*, 2017, **19**, 3800-3806.
27. L.-Å. Näslund, C. M. Sánchez-Sánchez, Á. S. Ingason, J. Bäckström, E. Herrero, J. Rosen and S. Holmin, *The Journal of Physical Chemistry C*, 2013, **117**, 6126-6135.
28. A. Tricoli, M. Graf and S. E. Pratsinis, *Advanced Functional Materials*, 2008, **18**, 1969-1976.
29. L. S. Santos, R. Landers and Y. Gushikem, *Talanta*, 2011, **85**, 1213-1216.

30.   H. J. Monkhorst and J. D. Pack, *Physical review B*, 1976, **13**, 5188.
31.   G. Henkelman, B. P. Uberuaga and H. Jónsson, *The Journal of chemical physics*, 2000, **113**, 9901-9904.
32.   J. Rossmeisl, A. Logadottir and J. K. Nørskov, *Chemical physics*, 2005, **319**, 178-184.
33.   NIST, *National Institutes of Standards and Technology, Gaithersburg, MD*, 2012.
34.   E. Sanville, S. D. Kenny, R. Smith and G. Henkelman, *Journal of computational chemistry*, 2007, **28**, 899-908.